Microwave Imaging Using a Disordered Cavity with a Dynamically Tunable Impedance Surface

Timothy Sleasman, Mohammadreza F. Imani, Jonah N. Gollub, and David R. Smith

Phys. Rev. Applied **6**, 054019 — Published 29 November 2016

DOI: 10.1103/PhysRevApplied.6.054019

Microwave Imaging Using a Disordered Cavity with a Dynamically Tunable Impedance Surface

Timothy Sleasman,* Mohammadreza F. Imani,† Jonah N. Gollub, and David R. Smith
Center for Metamaterials and Integrated Plasmonics, Duke University,
Department of Electrical and Computer Engineering, Durham NC, 27708
(Dated: October 20, 2016)

We perform microwave imaging using a dynamically reconfigurable aperture based on a tunable, disordered cavity. The electrically-large cavity is cubic, with a spherical-deformation, and supports a multitude of distinct electromagnetic modes that vary as a function of excitation frequency. With a set of irises introduced into one wall of the cavity, the cavity modes couple to spatially-distinct radiative modes that vary as a function of the driving frequency. To increase the diversity of the radiated fields, we replace one of the cavity walls with a variable impedance surface consisting of a set of varactor-populated mushroom structures grouped into pixels. The reflection phase of each pixel is independently changed with application of a voltage bias, effectively altering the surface impedance. We demonstrate high-fidelity imaging and examine the role of the impedance-tunable boundary condition, revealing superior performance in comparison with just frequency-diverse measurements. We also demonstrate single-frequency imaging, which could significantly reduce the demands on the required microwave source. The dynamic cavity imager may find relevance in security screening, through-wall imaging, biomedical diagnostics, and radar applications.

I. INTRODUCTION

Fast, high-resolution, and low-cost microwave imaging is highly desirable in a variety of applications including security screening [1], biomedical diagnostics [2–4], and synthetic aperture radar (SAR) [5, 6]. Conventional radio frequency (RF) hardware, however, has proven to be a limiting factor in the deployment of such systems. Most conventional RF imaging systems rely on mechanical scanning, electronic beam steering, or massive transmit-receive arrays [7–9]—technologies that are expensive or require long acquisition times. RF imaging systems based on computational imaging approaches [10–15] represent viable alternatives to these more established technologies. Such systems are capable of leveraging unconventional measurements and reconstruction algorithms to recover scene information. In one approach, a series of spatially-diverse patterns illuminate a scene, multiplexing its contents into a sequence of measurements that are then decoded in post-processing. By leveraging increasingly powerful processing, computational imaging shifts the burden of imaging from the physical layer to software, significantly expanding the hardware design space while enabling fast, high-quality image reconstruction.

The crux of computational imaging lies in generating a sequence of diverse waveforms, as illustrated in Fig. 1. For this purpose, unconventional platforms have been proposed and experimentally demonstrated in a variety of settings, from optical [16] and terahertz frequencies [17] to the acoustic regime [18, 19]. At microwave frequencies, metamaterial apertures and electrically-large cavities have shown great promise in producing such waveforms in the form of frequency-diverse radiation patterns. With metasurface apertures, for example, a waveguide is loaded with an array of radiating metamaterial resonators, whose resonance frequencies are randomly distributed over the band of operation [20–22]. As the driving frequency is swept, different subsets of the resonators radiate, producing complex, frequency-indexed patterns. These patterns are used in backscatter measurements to multiplex the spatial content of a scene, enabling high-quality images with fast acquisition times. However, with a metamaterial aperture the diversity of the generated patterns is limited by the quality (Q-) factor of the resonators and their intrinsic losses, which in turn limits the effective number of measurements and the information that can be recovered from the scene.

To circumvent the Q-factor limitations, electrically-large cavities have been proposed. Electrically-large cavities and disordered media have been a topic of much interest in a wide array of fields [16, 23–37]. This interest is primarily due to the fact that cavities possess high quality factors and, when electrically-large and deformed, can support a multitude of irregular eigenmodes. In [29], this feature of cavities has been used to emulate quantum mechanical chaos—a simple method to experimentally examine complicated phenomena. At microwave frequencies, large cavities have long been used for electromagnetic compatibility (EMC) tests [30–34]. Recently, high-efficiency energy transfer from a large cavity to a resonant receiver has been proposed based on coupled mode theory and has been experimentally demonstrated [35, 36].

The use of deformed cavities for imaging purposes was first suggested and demonstrated in ultrasonic 3D tomography [38]. In this work, time reversal of ultrasonic waves was used to concentrate energy at desired locations. Similar ideas were later proposed and demonstrated in other media which exhibit a high density of resonant states [39].

* These authors contributed equally; sleasmant@gmail.com
† These authors contributed equally

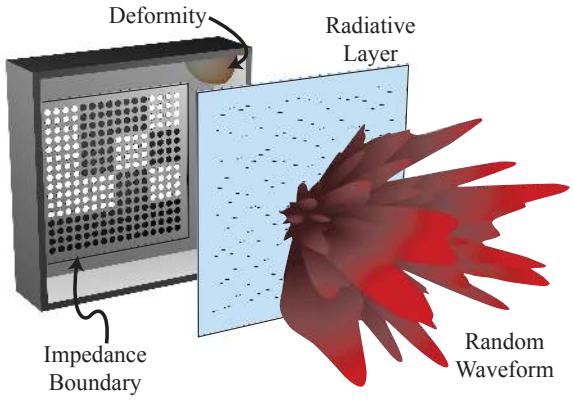

FIG. 1. Depiction of a disordered cavity with a tunable boundary condition. The perforated wall is displayed away from the cavity and a numerical example of a radiation pattern is plotted.

The idea of using deformed media and a high density of states to retrieve spatial content was later introduced at microwave frequencies [40]. In this work, distinct modes formed within a disordered cavity were projected into a scene by introducing an array of irises into one of the cavity walls, as depicted in Fig. 1. The resulting waveforms show significant spatial variation as a function of frequency, enabling retrieval of a scene's reflectivity via a frequency sweep.

While volumetric and planar cavities have both shown promise in experiments [37, 40–43], they require a large operational bandwidth. Large frequency bandwidth, though required in part for range resolution [44, 45], may not be readily available in practice and can complicate the design of a coherent RF transceiver. Furthermore, the generation of frequency-diverse patterns relies on achieving a high Q-factor, which is inversely proportional to cavity losses; since radiation is the primary cavity loss mechanism, there is an inherent upper limit on the performance of any frequency-diverse aperture [46]. To illustrate this limitation, let us assume a cavity possesses a large Q-factor. For this case, we assume that the amplitude and phase of the electromagnetic field exciting each radiator at each frequency are random. As a result, each radiator obtains a unique measurement of the scene; in other words, in the ideal case of large quality factor, the number of unique measurement modes generated via frequency diversity is determined by the number of radiators. As such, it is desired to increase the number of radiators to obtain a larger number of distinct radiation patterns and hence measurements; however, the insertion of additional radiators increases the radiative loss, thus reducing the Q-factor and deteriorating the diversity of the interrogating waveforms. For example, the quality factor of the deformed cavity used in [40] was reduced from 45,000 to 350 as a result of the introduction of radiating irises.

To mitigate the limitations inherent to frequency diversity, a tuning mechanism can be added to the system. In [47–49], PIN diodes were integrated within metamaterial resonators to construct a one dimensional (1D) metasurface dynamic aperture. These diodes, addressed independently, rendered each resonator *on* or *off* depending on an applied DC voltage. In this manner, the DC circuitry selects different subsets of elements to radiate, resulting in distinct radiation patterns without dependence on frequency sweeps. Using the 1D dynamic metasurface, high-fidelity imaging of simple objects in two-dimensions (range and one cross-range variable) has been experimentally demonstrated at real-time frame rates [49]. It is important to note that dynamic metasurfaces are able to alter their radiation patterns through simple, low-cost circuitry and do not require active components such as phase shifters or amplifiers, which are expensive, bulky, and consume large amounts of DC power [50].

The fundamental operation of the dynamic metasurface used in [47–49] lies in tuning the resonances of the metamaterial elements to alter the radiation patterns. As a result, the aperture's performance is still limited by the resonant losses of the metamaterial elements. For example, the number of *on* and *off* elements in [49] had to be chosen carefully to ensure sufficient radiated power with an appropriately large effective aperture. To overcome the losses associated with the diode-loaded metamaterial elements, multiple feed points were required to ensure the aperture was fully sampled.

To overcome the limitations of frequency-diverse systems as well as dynamic apertures, we propose a tunable cavity that possesses the advantages of both. In this cavity, depicted in Fig. 1, we incorporate a tunable impedance surface rather than modifying the responses of the independent radiators. By changing the boundary's impedance, we alter the cavity's modal distribution and generate distinct radiation patterns without changing the frequency. We highlight the design of the impedance boundary condition and discuss its integration within the proposed cavity. We experimentally confirm the role of the boundary-tuned cavity and its superior performance over the frequency-diverse aperture. We also present an imaging system deploying the proposed tunable cavity, demonstrating high-quality 3D images. To further emphasize the utility of tunable cavities, we perform single-frequency imaging of planar objects. We conclude by discussing the potential outlook of this device and its prospective applications.

II. TUNABLE CAVITY DESIGN

The cavity used in this paper is similar to the ones used in [38, 40]. The present structure is depicted in Fig. 2 and consists of a metalized, cuboid of dimensions 11 cm $\times$ 11 cm $\times$ 5.5 cm ($\sim 7\lambda \times 7\lambda \times 4\lambda$, where λ is 1.5 cm, corresponding to a frequency of 20 GHz). One corner is deformed into the shape of a sphere octant, with radius 3 cm (2λ), to perturb the rectangular eigenmodes. This

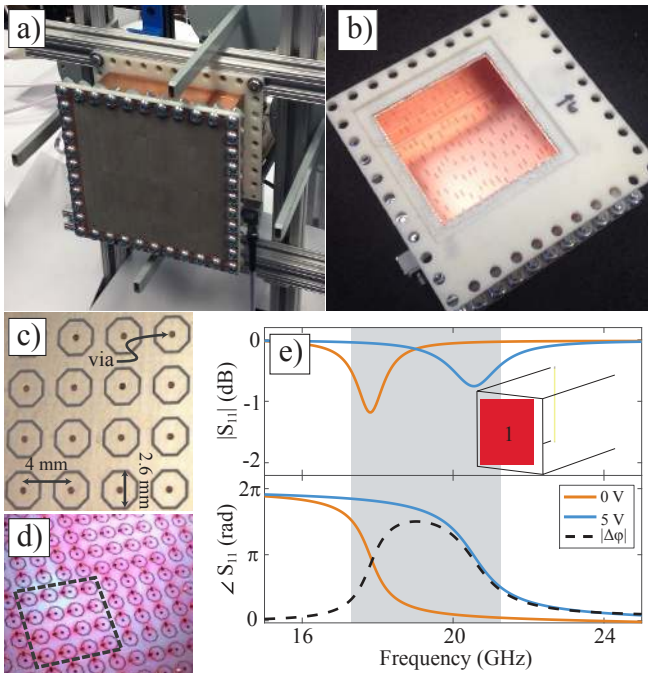

FIG. 2. a) The cavity implemented in the imaging configuration, including four open-ended waveguide receivers. A network analyzer and mechanical switch are situated behind the aperture to take the measurements from the different receivers. b) The interior of the cavity when the impedance surface is removed. c) A zoom in of the particular mushroom structure and d) a highlighted pixel on the varactor-populated impedance surface. e) The full-wave simulation domain and results for a mushroom unit cell.

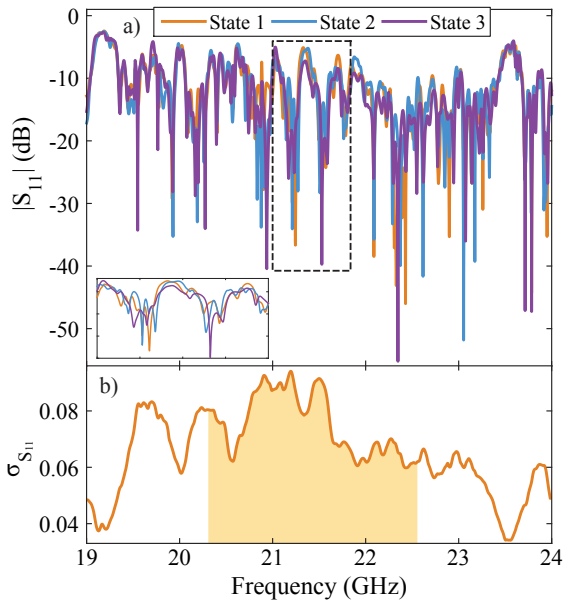

FIG. 3. a) Return loss of the perforated cavity with a dense frequency sampling. Three example states are shown as well as a zoom in (contained by the dashed box). b) The standard deviation of the return loss is also plotted for a set of 100 measurements and the bandwidth used for imaging is highlighted.

cavity is excited by a WR42 rectangular waveguide (K band frequency range).

In contrast to the cavities in [38, 40], one wall of this cavity is left as an open window for incorporation of a tunable-impedance boundary plate. The tunable plate, depicted in Fig. 2, has 8 cm × 8 cm lateral dimensions, is made of 1.5 mm thick Rogers 4003C substrate (dielectric constant of 3.55 and loss tangent of 0.0027), and contains a pixelated array of mushroom structures which each contain a varactor. Mushroom structures, or high impedance surfaces, were first used as a method to emulate the response of perfect magnetic conductors (PMC) [51]. Since then, various designs with different properties, both passive and dynamic [52], have been proposed.

Here, we use mushroom structures consisting of an octagon inscribed in a 2 mm diameter circle, which are surrounded by a 0.3 mm gap and have a via of 0.5 mm diameter connecting to the ground plane. The size of the mushrooms and the particular varactor (MACOM MAVR-011020-1411) were chosen such that the transition of the mushroom structure from perfect electric conductor (PEC) to PMC happens within the K band. To accomplish this condition, a single mushroom was simulated in a full-wave electromagnetic solver, CST Microwave Studio. The reflection phase and magnitude, depending on the capacitance of the varactor, are plotted in Fig. 2e. As can be seen, the reflection phase of the surface changes through a full rotation of 0 to 2π (taking on the behavior of both PEC and PMC) in the frequency range 17.5 GHz–21.5 GHz. As expected, the reflected signal's amplitude remains close to unity over the band of operation. While the simulation setting assumes normal plane wave incidence and an infinite array of mushrooms structures, its results ensure variation of the reflected phase for practical cases of oblique incidence and finite array size. It is important to note that we are not interested in obtaining an exactly prescribed amount of return phase, but rather in causing tangible variations, which essentially change the cavity's boundary condition and the resulting eigenmodes.

Once the design of the mushroom structure is finalized, a 4×4 array of mushrooms is grouped together to constitute a pixel—a group of mushrooms all controlled by the same voltage. Sixteen such pixels are then tessellated to form a 4×4 grid that occupies the cavity wall. Each pixel can be addressed separately using a (0 or 5 V) DC voltage dictated by an Arduino microcontroller. The total number of sixteen pixels allows for $2^{16} = 65{,}536$ distinct surface impedance states. The varactors are 90° rotated from each other in neighboring pixels to ensure coupling to both polarizations. The need to address both polarizations arises from the nature of the cavity modes. In a disordered cavity, a plane wave decomposition at each point consists of a combination of arbitrary wavevectors

and polarizations; as a result, the deformed electrically-large cavity does not possess a dominant field polarization.

Incorporation of such a tunable impedance boundary into the cavity offers two crucial advantages: 1) the tuning mechanism is separated from the radiating layer, enlarging the design space for the radiative layer. In other words, the choice of radiative elements can be designed to further optimize the performance for the intended application. 2) Such a cavity supports a multitude of distinct modes, which can be tuned with modification of the impedance boundary condition. The dynamic impedance wall allows the generation of highly-distinct waveforms without trade-offs concerning the number of radiating elements, bandwidth, or cavity quality factor. Ultimately, the number of independent measurement modes for an aperture should be dictated by the space-bandwidth product [53, 54] rather than Q-factor or design-specific limitations. To form the aperture, one side of the cavity is perforated with 150 randomly distributed slots (see Fig. 1 and 2). The slots are designed to radiate into a single polarization at K band with minimal losses. Use of such simple and efficient radiators is an important advantage associated with disordered cavity resonators.

We note that a cavity with a tunable impedance boundary has also been utilized in [55, 56]. In [55], the tuning of a spatial phase modulator [57] was used to form a focal spot in a desired location for improving communication between two antennas placed within a reverberating cavity (a conventional room in this case). In [56, 58], a combination of electronically-tunable and mechanical stirrers was used to shape the waveforms within the cavity. By contrast, here we utilize the tunable boundary to form diverse radiation patterns outside the cavity for computational imaging purposes. Given the requirements of this application, the designed cavity and the impedance boundary are distinct from those reported in [55–57]. Additionally, a rudimentary version of a tunable cavity was demonstrated in [59] but this device was also mechanically actuated. It is also worth noting that while the scrambling of a cavity's fields has been demonstrated for various purposes using mechanical stirrers, this approach is slow and may exhibit inconsistencies or fluctuations, drawbacks which are prohibitive for our application.

Once the deformed cavity was fabricated, it was examined using a network analyzer (Agilent E8364C). In the first set of measurements, the return loss of the tunable cavity was measured for 100 different states of the impedance boundary. The entire K band (17.5 GHz–26.5 GHz) was sampled at intervals of 1.406 25 MHz (6401 points). As an example, the return loss for three different tuning states is plotted in Fig. 3. A multitude of resonances (represented by the dips in the return loss) can be observed for all three states. In fact, when there are no radiation losses, the closed cavity can support a much larger number of modes, each of which has a narrow linewidth (high quality factor). Due to the radiation losses, the spectral linewidths of the modes have increased and many of the dips have merged into each other.

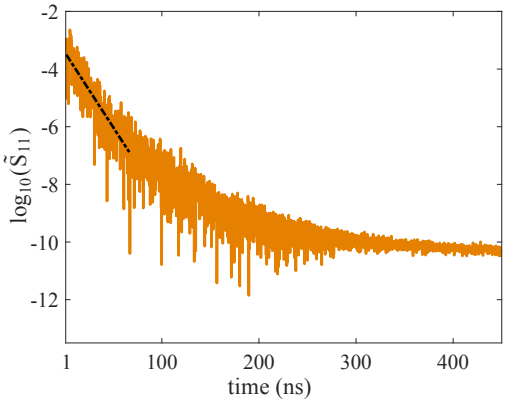

FIG. 4. Time domain plot of the return loss (in log) along with a fitted line from which the experimental Q can be calculated.

This phenomenon can be confirmed by calculating the quality factors of the loaded (radiating) and closed (non-radiating) cavity. In the literature, it is common to invoke the thermodynamic analog of the reverberating chamber to calculate its unloaded quality factor through $Q = 16V\pi^2 f^3/c^3$ [31, 32]. Using this formula, the unloaded quality factor is estimated to be $Q \approx 30{,}000$. The Q of the loaded cavity (i.e. with the radiative layer) is computed using the decay rate of its impulse response [31, 43]. To do this, the Fourier transform of the return loss is taken over the entire K band with sufficient sampling so that there is no aliasing in the time domain response—depicted in Fig. 4. The exponential decay rate, α, of the time domain return loss ($\widetilde{S}_{11}(\tau) = e^{-\alpha\tau}$) can be calculated by fitting the curve in Fig. 4 with a linear regression. Once the decay constant α is computed it is inserted into $Q = f_c\pi/\alpha$ (where $f_c = 20\,\text{GHz}$ is the center frequency) to obtain the quality factor. For the current cavity, this process results in $Q \approx 600$, which is much smaller than the unloaded quality factor. This observation once again exemplifies the trade-off between the radiation and the correlation of the modes.

Examining the return loss results in Fig. 3, we also observe significant variation in S_{11} as a function of tuning states within the middle of the K band. These variations reveal two important factors: 1) through changing the boundary, we are altering the modal distribution within the cavity, as manifested by the changing locations of the resonant dips. This variation, which is explicated in [56], enables us to alter the radiation patterns generated by the device. 2) The frequency range over which these variations are greatest is 19.5 GHz–23.5 GHz. To determine this range, we calculated the statistical standard deviation of S_{11} for 100 states, $\sigma_{S_{11}}$. This deviation is plotted in Fig. 3 as a function of frequency. Clearly, the standard deviation is the highest over the

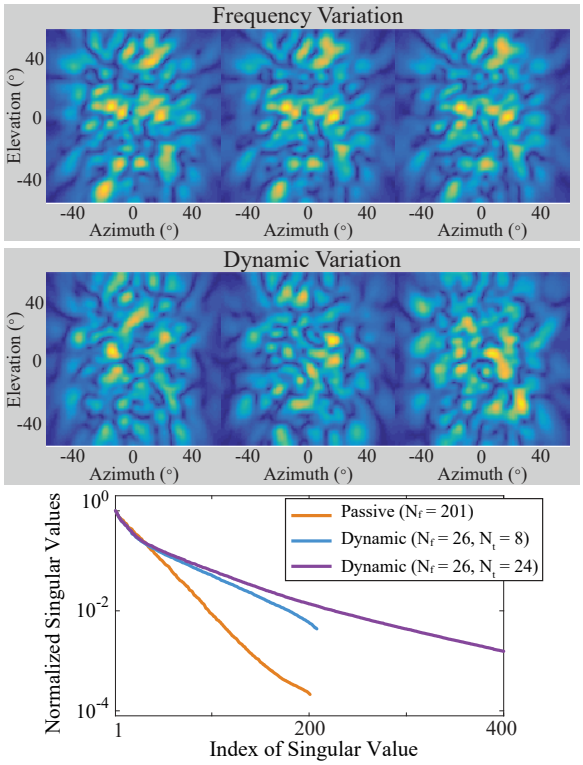

FIG. 5. Variation in the radiated electric field for three neighboring frequencies (separated by 11.25 MHz) and three random tuning states (all at 20.875 GHz), all plotted with the same linear scale as a function of azimuth and elevation. The data is transformed from the near-field measurements and all plots are normalized to the same scale. A more quantitative perspective is given by the SV spectrum which is plotted below the fields for the passive and dynamic apertures.

range 19.5 GHz–23.5 GHz. This frequency range is close to that of the designed impedance surface (17.5 GHz–21.5 GHz); the slight frequency shift can be attributed to fabrication and component tolerance.

The results presented in Fig. 3 verify that the tunable boundary condition is responsible for altering the cavity's modes. Next, the radiative near-field of the cavity is scanned for different states and at frequency intervals of 11.25 MHz over 20.3125 GHz–22.5625 GHz (resulting in 201 frequency points) using an open-ended waveguide; a step size of 5 mm ($<\lambda_{min}/2$) is used to completely characterize the radiated fields. The frequency step size is increased from that used for the S_{11} experiments so that the near-field scanning and imaging measurements can be performed in a timely manner. Furthermore, using the analysis in [46], the number of useful modes or frequency points for such a cavity operated without dynamic tuning is estimated to be $QB/f_c \approx 146$, where B is the bandwidth. Our choice of 201 frequency points guarantee we are capturing all the distinct radiated modes generated by this cavity.

The near-field scan data is then used in conjunction with surface equivalence principles [60] to compute the radiation patterns everywhere in the scene for every state of the impedance boundary and every frequency point. Computed radiation patterns for three different frequencies (constant tuning states) and three different tuning states (constant driving frequency) are plotted in Fig. 5 in a plane at a distance of 50 cm. The former represents frequency-diverse radiation patterns (as would be the case in a passive cavity) and the latter exemplifies dynamically-tuned radiation patterns. Evidently, utilizing the tuning results in less correlation between the radiation patterns (manifested as higher spatial variation). It should also be noted that in both cases the radiation patterns exhibit many lobes (instead of the one directive main lobe conventionally used) so that they illuminate a large portion of the scene. While this results in lower reflected signal and a decrease in the signal to noise ratio (SNR), it is fundamentally necessary for the multiplexing approach of computational imaging. In applications where imaging is completed at large distanceon the order of kilometers for synthetic aperture radarSNR would become a greater concern, but in the near-field application that we consider here the hardware provides sufficient SNR even with the low gain radiation patterns.

To better quantify the variation of the radiated fields, we populate a matrix with the calculated radiation patterns. Each row of the resulting matrix consists of the radiated electric field for a given tuning state and driving frequency. As a result, the total number of rows, N, is the multiplication of the number of tuning states, N_t, and the number of frequency points, N_f. A singular value decomposition (SVD) of this matrix reveals the degree of correlation among its rows (or radiation patterns). Recall that diversity among radiation patterns enables multiplexing of unique information during imaging. A flat singular value spectrum, indicates high orthogonality between rows while a rapidly decaying singular value spectrum indicates severely correlated radiation patterns. The SV spectrum for radiation patterns generated by the passive (with $N = N_f = 201$) and dynamic cavities (with $N_f = 26$, $N_t = 8$, resulting in $N = 208$) are plotted in Fig. 5. The same bandwidth, 20.3125 GHz–22.5625 GHz, is used in both cases with the dynamic case having courser sampling. Clearly, the SV spectrum of the tunable cavity exhibits significantly less correlation. Another important factor is that the dynamic cavity allows us to use a larger quantity of distinct patterns, as is evidenced by Fig. 5 where we have also plotted the case with three times as many tuning states. Eventually the amount of obtainable information using the tunable disordered cavity saturates, as will be seen in the discussion of single-frequency imaging.

The results presented in Fig. 5 indicate that the radiation patterns generated by the tunable cavity can interrogate the entire imaging domain and encode its spatial content into simple backscattered measurements as a function of tuning state or frequency or both. The efficacy of this proposal is examined in the next section and the two methods for image retrieval are contrasted, fur-

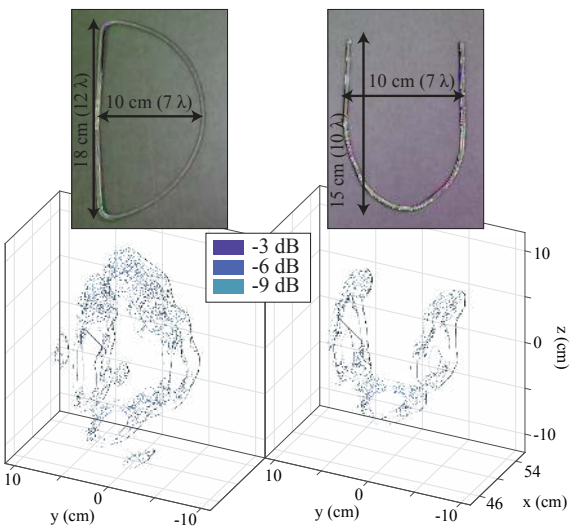

FIG. 6. Reconstructed 3D images of the letters D and U obtained using 26 frequency points and 30 tuning states.

ther highlighting the enhanced performance made available by the tunable boundary condition.

III. IMAGING RESULTS

The tunable cavity is implemented in the imaging configuration pictured in Fig. 2. In this setting, the cavity acts as a transmitting aperture interrogating a scene under test. The signal backscattered by the scene is collected by four open-ended waveguides situated around the perimeter of the cavity. The cavity is connected to port 1 of a network analyzer and the probes are connected to port 2. The signal paths from the receiving probes to the receive port of the network analyzer are separated using a mechanical switch. The measured S_{21} is then a signal initiated at the transmitting port, radiated by the tunable cavity, reflected by the scene, and collected by receiving probes. This process is repeated sequentially for the four probes (four signal paths). For each probe, the impedance surface is cycled through a set of patterns with an applied voltage to generate the various radiation patterns. The open-ended waveguides have a radiation pattern that can be estimated by modeling the aperture as a point magnetic dipole [61]. Electric fields in the domain are then calculated with the appropriate Green's function.

The measured S_{21} thus represents the backscattered signal, which is post-processed to reconstruct an image of the scene. To do this, the relationship between the scattered signal and radiation patterns of the system's apertures needs to be described. Assuming first Born approximation (weak scatterers and single scattering events) and diffraction-limited resolution, this relationship is formulated as [22]

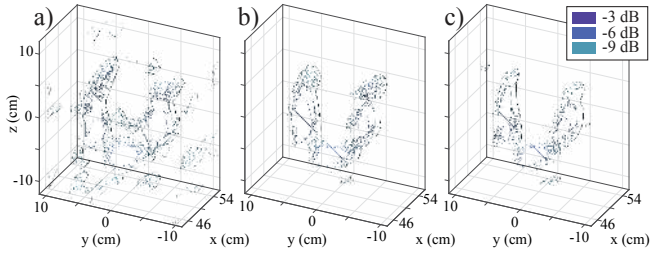

FIG. 7. a) Passive-mode reconstruction of the letter U, obtained with 201 frequency points. b) Dynamic reconstruction with approximately the same number of measurements ($N = 208$) and c) dynamic result with half as many measurements ($N = 104$).

$$\mathbf{g} = \mathbf{H}\mathbf{f} \tag{1}$$

where $\mathbf{g}$ is the measured signal, $\mathbf{f}$ is the reflectivity of the scene (the quantity to be estimated), and $\mathbf{H}$ is the sensing matrix. The $\mathbf{H}$ matrix is composed of the waveforms generated by the transmitting and receiving apertures. Expanding a specific entry of $\mathbf{g}$ and row of $\mathbf{H}$ we can see that the measurements relate to the scene reflectivity as

$$g_i = \Sigma_j H_{ij} f_j = \Sigma_j (\mathbf{E}_i^T(\mathbf{r}_j) \cdot \mathbf{E}_i^R(\mathbf{r}_j)) f_j. \tag{2}$$

In this equation the $\mathbf{H}$ matrix is represented in terms of the transmitter's and receiver's fields, $\mathbf{E}_i^T$ and $\mathbf{E}_i^R$, for the i-th mode. The index i revolves through frequencies, tuning states, and different receive antennas to count all of the interrogating waveforms. The $\mathbf{r_j}$ are the locations in the scene and j sweeps through the entire region of interest.

Equation 1 can be used to estimate $\mathbf{f}$. In practice, $\mathbf{H}$ is not square and a true mathematical inverse does not exist. Even in the case of square $\mathbf{H}$, direct inversion is not advised due to presence of noise. As a result, we use an iterative least squares solver, GMRES, to estimate $\mathbf{f}$. The specific implementation of the reconstruction algorithm is an active area of research and beyond the scope of this paper. As we are agnostic to the choice of reconstruction, the requirement of diversity among the rows of $\mathbf{H}$ is essential for high-quality image formation.

We start our experiments by first examining the ideal case, when a large number of tuning masks, $N_t = 30$, and frequency points, $N_f = 26$, are used to image different objects. The letters D and U, formed using thin metallic wire, have been used as the targets under investigation. The reconstructed images are shown in Fig. 6. Both objects are located at a depth of 50 cm and are clearly resolved. These images confirm the ability of the boundary-tuned cavity to retrieve high-quality images.

Next, we focus on identifying the role of the tunable impedance boundary in retrieving scene information. To do this, the letter U is imaged with the cavity operating in passive mode (mere frequency diversity, with

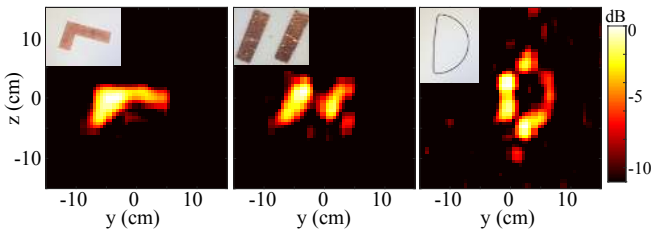

FIG. 8. Images of three objects taken with a single frequency point. Reconstructions with 200 tuning states of planar objects located at 50 cm.

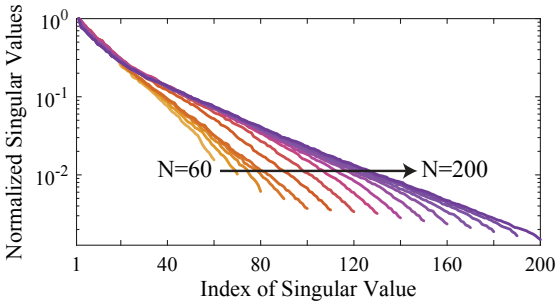

FIG. 9. Comparison among different quantities of tuning states. The SV spectra grade from 60 to 200 tuning states (in steps of 20) and the information content saturates within this span.

$N = N_f = 201$) as well as dynamic mode (with $N_t = 8$ and $N_f = 26$, resulting in $N = 208$ total measurements). The results are plotted in Fig. 7. In the passive case the diodes are all set so that the mushroom structure acts as a PEC. To keep a fair comparison, the number of measurements (i.e. the number of rows of H) is kept roughly the same in both cases. Evidently, the frequency-diverse cavity can resolve the objects, but with lower quality, while the tunable cavity can form a clear image of the targets with the same number of measurements. In fact, even when the number of measurements is halved ($N_t = 4$, such that $N = 104$), the dynamic cavity can obtain higher-quality images. This once again exemplifies the powerful capabilities of the dynamic cavity.

In all of the images reported above, the bandwidth has been kept at 20.3125 GHz–22.5625 GHz, the same as that used for the SVD analysis. This is done to keep the range resolution, predominantly retrieved through frequency bandwidth [44], identical for the passive and dynamic cases. If a larger bandwidth is used the results for the passive case will be improved; however, in many applications a large frequency bandwidth may not be available or may complicate the design of the RF transceiver. The reduction in frequency sampling for the dynamic case leads to a decreased unambiguous range (UR). This is not concerning for the tunable cavity since many frequency-diverse systems are extremely oversampled and have an UR which is significantly larger than the actual region of interest [21, 40, 42, 43]. Additionally, in many scenarios the location of the target is constrained (for example in screening of objects on a predetermined platform or in spaceborne SAR systems) to a known range of distances. If no range information is desired or if the object is confined to a plane, a single frequency can be used to obtain images. In contrast to the frequency-diverse implementations, the dynamic cavity at hand offers such capability. This idea is demonstrated in Fig. 8 where 2D images of different targets have been reconstructed using $N_t = 200$ states and a single frequency (21.4375 GHz).

The results presented in Figs. 6-8 confirm the utility of the tunable cavity in computational imaging settings. In particular, they demonstrate the ability of the tunable cavity to generate distinct radiation patterns, even when the cavity's quality factor is significantly reduced by radiation losses. In other words, the performance of the tunable cavity is not limited by the inexorable trade-off between the number of radiating slots and the quality factor [46]. This notion raises an important question: what limits the number of distinct radiation patterns that this cavity can generate? To answer this question, we note that any radiated pattern is the superposition of fields generated by the radiative slots. As such, the total number of possible distinct patterns is bounded by the number of radiative slots. To illustrate this point, we have computed the SV spectra for different numbers of states at single frequency and plotted them in Fig. 9. Evidently the information content saturates somewhere around 150 tuning states which is comparable to our 150 slots.

This saturation feature can also be observed in the single frequency reconstructions depicted in Fig. 10. In this figure, the dynamic cavity operating at a single frequency is used to image a sub-diffraction-limited scatterer (a ball bearing of diameter 1.6 cm). As we decrease the number of states from 200 to 50, the image quality degrades slightly. However, above 150 states, the image quality remains virtually identical. If desired, more slots could be introduced into the radiative layer and the number of useful radiation patterns could be increased further. This process will ultimately become limited by the space bandwidth product associated with the aperture's physical dimension and the operating frequency. Probing this limit is an interesting prospect left for a future work.

IV. SUMMARY AND FUTURE DIRECTIONS

The results presented in this paper establish the tunable, disordered cavity as a promising device to generate distinct radiation patterns for computational imaging purposes. In particular, it was shown that separating the radiative layer and tuning mechanism significantly loosens the constraint that resonant and radiative losses impose on performance. In the future, various improvements can be added to this device. For example, here we addressed the varactors using only 0 V and 5 V DC while we could continuously vary the voltage (0 V–5 V)

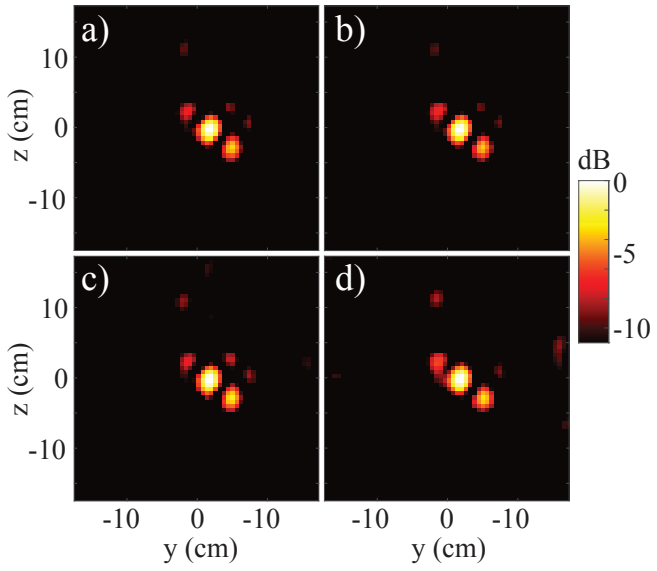

FIG. 10. Single-frequency images of a sub-resolution scatterer (a centered 1.5 cm diameter sphere) with different quantities of measurements. Quality remains the same between a) 200 and b) 150 but slowly degrades for c) 100 and d) 50 measurements. Note that the angular skew in the PSF is induced by the asymmetric alignment of the receiving antennas.

to increase the control over the radiated fields. The tuning mechanism can also be modified to employ thin-film transistors or liquid crystals.

This device can also be envisioned in a planar form factor to simplify the fabrication process and enable low-profile deployment. Alternatively, the perforated wall of the cavity can take on a shape conformal to the imaging domain, making them attractive devices for application in biomedical systems. Such an implementation could be of use in breast cancer detectors or could be employed to form a focal spot within a certain layer of tissue for device charging or heat application. Structures similar to the demonstrated device have shown promise in telecommunications and wireless power transfer, where they have relied on a large cavity (such as a room) and operated within the reverberating medium. The presented tunable cavity combines the features of both tuning and frequency-mixing properties and can easily be used for generating on-demand hot spots for telecommunication or wireless power transfer purposes. Given these promising outlooks, we believe tunable mode mixing cavities, either in volumetric or planar form factors, will find many applications in security screening, biomedical diagnostics, telecommunications, and wireless power transfer, among many others.

ACKNOWLEDGMENTS

This work was supported by the Air Force Office of Scientific Research (AFOSR, Grant No. FA9550-12-1-0491).

[1] D. M. Sheen, D. L. McMakin, and T. E. Hall, "Three-dimensional millimeter-wave imaging for concealed weapon detection," IEEE Trans. Microw. Theory Techn. **49**, 1581–1592 (2001).

[2] P. M. Meaney, K. D. Paulsen, and J. T. Chang, "Near-field microwave imaging of biologically-based materials using a monopole transceiver system," IEEE Trans. Microw. Theory Techn. **46**, 31–45 (1998).

[3] M. Haynes, J. Stang, and M. Moghaddam, "Microwave breast imaging system prototype with integrated numerical characterization," Journal of Biomedical Imaging **2012**, 2:2–2:2 (2012).

[4] E. J. Bond, X. Li, S. C. Hagness, and B. D. Van Veen, "Microwave imaging via space-time beamforming for early detection of breast cancer," Antennas and Propagation, IEEE Transactions on **51**, 1690–1705 (2003).

[5] M. Dehmollaian and K. Sarabandi, "Refocusing through building walls using synthetic aperture radar," Geoscience and Remote Sensing, IEEE Transactions on **46**, 1589–1599 (2008).

[6] Y. Oh, K. Sarabandi, and F. T. Ulaby, "An empirical model and an inversion technique for radar scattering from bare soil surfaces," IEEE Transactions on Geoscience and Remote Sensing **30**, 370–381 (1992).

[7] S. S. Ahmed, A. Schiessl, F. Gumbmann, M. Tiebout, S. Methfessel, and L. P. Schmidt, "Advanced microwave imaging," IEEE Microwave Magazine **13**, 26–43 (2012).

[8] B. Gonzalez-Valdes, Y. Alvarez, S. Mantzavinos, C. M. Rappaport, F. Las-Heras, and J. A. Martinez-Lorenzo, "Improving security screening: A comparison of multistatic radar configurations for human body imaging," IEEE Antennas and Propagation Magazine **58**, 35–47 (2016).

[9] B. Gonzalez-Valdes, G. Allan, Y. Rodriguez-Vaqueiro, Y. Alvarez, S. Mantzavinos, M. Nickerson, B. Berkowitz, J. A. Martinez-Lorenzo, F. Las-Heras, and C. M. Rappaport, "Sparse array optimization using simulated annealing and compressed sensing for near-field millimeter wave imaging," Antennas and Propagation, IEEE Transactions on **62**, 1716–1722 (2014).

[10] D. L. Donoho, "Compressed sensing," IEEE Transactions on Information Theory **52**, 1289–1306 (2006).

[11] D. J. Brady, K. Choi, D. L. Marks, R. Horisaki, and S. Lim, "Compressive holography," Opt. Exp. **17**, 13040–13049 (2009).

[12] D. J. Brady, *Optical imaging and spectroscopy* (John Wiley & Sons, 2009).

[13] S. Caorsi, A. Massa, and M. Pastorino, "A computational technique based on a real-coded genetic algorithm for microwave imaging purposes," IEEE Transactions on Geoscience and Remote Sensing **38**, 1697–1708 (2000).

[14] M. Rossi, A. M. Haimovich, and Y. C. Eldar, "Spatial compressive sensing for mimo radar," IEEE Transactions on Signal Processing **62**, 419–430 (2014).

[15] Y. C. Eldar and G. Kutyniok, *Compressed sensing: theory and applications* (Cambridge University Press, 2012).

[16] A. Liutkus, D. Martina, S. Popoff, G. Chardon, O. Katz, G. Lerosey, S. Gigan, L. Daudet, and I. Carron, "Imaging with nature: Compressive imaging using a multiply scattering medium," Scientific reports **4** (2014).

[17] C. M. Watts, D. Shrekenhamer, J. Montoya, G. Lipworth, J. Hunt, T. Sleasman, S. Krishna, D. R. Smith, and W. J. Padilla, "Terahertz compressive imaging with metamaterial spatial light modulators," Nature Photonics (2014).

[18] Y. Xie, T. Tsai, A. Konneker, B. Popa, D. J. Brady, and S. A. Cummer, "Single-sensor multispeaker listening with acoustic metamaterials," Proceedings of the National Academy of Sciences **112**, 10595–10598 (2015).

[19] F. Lemoult, M. Fink, and G. Lerosey, "Acoustic resonators for far-field control of sound on a subwavelength scale," Phys. Rev. Lett. **107**, 064301 (2011).

[20] J. Hunt, T. Driscoll, A. Mrozack, G. Lipworth, M. Reynolds, D. Brady, and D. R. Smith, "Metamaterial apertures for computational imaging," Science **339**, 310–313 (2013).

[21] J. Hunt, J. Gollub, T. Driscoll, G. Lipworth, A. Mrozack, M. S. Reynolds, D. J. Brady, and D. R. Smith, "Metamaterial microwave holographic imaging system," J. Opt. Soc. Amer. A **31**, 2109–2119 (2014).

[22] G. Lipworth, A. Mrozack, J. Hunt, D. L. Marks, T. Driscoll, D. Brady, and D. R. Smith, "Metamaterial apertures for coherent computational imaging on the physical layer," J. Opt. Soc. Amer. A **30**, 1603–1612 (2013).

[23] A. Derode, A. Tourin, J. de Rosny, M. Tanter, S. Yon, and M. Fink, "Taking advantage of multiple scattering to communicate with time-reversal antennas," Phys. Rev. Lett. **90**, 014301 (2003).

[24] A. Derode, A. Tourin, and M. Fink, "Random multiple scattering of ultrasound. 1. coherent and ballistic waves," Phys. Rev. E **64**, 036605 (2001).

[25] G. Lerosey, J. de Rosny, A. Tourin, and M. Fink, "Focusing beyond the diffraction limit with far-field time reversal," Science **315**, 1120–1122 (2007).

[26] O. Katz, P. Heidmann, M. Fink, and S. Gigan, "Non-invasive single-shot imaging through scattering layers and around corners via speckle correlations," Nature photonics **8**, 784–790 (2014).

[27] N. Garcia and A. Z. Genack, "Crossover to strong intensity correlation for microwave radiation in random media," Phys. Rev. Lett. **63**, 1678–1681 (1989).

[28] J. Wang and A. Z. Genack, "Transport through modes in random media," Nature **471**, 345–348 (2011).

[29] H. J. Stöckmann and J. Stein, "Quantum chaos in billiards studied by microwave absorption," Physical review letters **64**, 2215 (1990).

[30] P. Corona, G. Latmiral, E. Paolini, and L. Piccioli, "Use of a reverberating enclosure for measurements of radiated power in the microwave range," IEEE Transactions on Electromagnetic Compatibility **EMC-18**, 54–59 (1976).

[31] M. T. Ma, M. Kanda, M. L. Crawford, and E. B. Larsen, "A review of elecromagnetic compatibility/interference measurement methodologies," in *IEEE Proceedings*, Vol. 73 (1985) pp. 388–411.

[32] P. Corona, G. Ferrara, and M. Migliaccio, "A spectral approach for the determination of the reverberating chamber quality factor," IEEE transactions on electromagnetic compatibility **40**, 145–153 (1998).

[33] M. P. Robinson, J. Clegg, and A. C. Marvin, "Radio frequency electromagnetic fields in large conducting enclosures: effects of apertures and human bodies on propagation and field-statistics," IEEE transactions on electromagnetic compatibility **48**, 304–310 (2006).

[34] K. A. Remley, J. Dortmans, C. Weldon, R. D. Horansky, T. B. Meurs, C. Wang, D. F. Williams, C. L. Holloway, and P. F. Wilson, "Configuring and verifying reverberation chambers for testing cellular wireless devices," IEEE Transactions on Electromagnetic Compatibility **58**, 661–672 (2016).

[35] M. J. Chabalko and A. P. Sample, "Resonant cavity mode enabled wireless power transfer," Applied Physics Letters **105**, 243902 (2014).

[36] J. S. Ho, Y. Tanabe, S. M. Iyer, A. J. Christensen, L. Grosenick, K. Deisseroth, S. L. Delp, and A. S. Poon, "Self-tracking energy transfer for neural stimulation in untethered mice," Physical Review Applied **4**, 024001 (2015).

[37] M. F. Imani, T. Sleasman, J. N. Gollub, and D. R. Smith, "Analytical modeling of printed metasurface cavities for computational imaging," Journal of Applied Physics **120** (2016), http://dx.doi.org/10.1063/1.4964336.

[38] G. Montaldo, D. Palacio, M. Tanter, and M. Fink, "Building three-dimensional images using a time-reversal chaotic cavity," IEEE transactions on ultrasonics, ferroelectrics, and frequency control **52**, 1489–1497 (2005).

[39] F. Lemoult, G. Lerosey, J. de Rosny, and M. Fink, "Resonant metalenses for breaking the diffraction barrier," Physical review letters **104**, 203901 (2010).

[40] T. Fromenteze, O. Yurduseven, M. F. Imani, J. Gollub, C. Decroze, D. Carsenat, and D. R. Smith, "Computational imaging using a mode-mixing cavity at microwave frequencies," Appl. Phys. Lett. **106**, 194104 (2015).

[41] T. Fromenteze, C. Decroze, and D. Carsenat, "Waveform coding for passive multiplexing: Application to microwave imaging," IEEE Transactions on Antennas and Propagation **63**, 593–600 (2015).

[42] T. Fromenteze, E. L. Kpre, D. Carsenat, C. Decroze, and T. Sakamoto, "Single-shot compressive multiple-inputs multiple-outputs radar imaging using a two-port passive device," IEEE Access **4**, 1050–1060 (2016).

[43] O. Yurduseven, J. N. Gollub, D. L. Marks, and D. R. Smith, "Frequency-diverse microwave imaging using planar mills-cross cavity apertures," Opt. Exp. **24**, 8907–8925 (2016).

[44] M. Soumekh, *Fourier array imaging* (Prentice-Hall, Inc., 1994).

[45] O. Yurduseven, M. F. Imani, H. Odabasi, J. Gollub, G. Lipworth, A. Rose, and D. R. Smith, "Resolution of the frequency diverse metamaterial aperture imager," Progress In Electromagnetics Research **150**, 97–107 (2015).

[46] D. L. Marks, J. N. Gollub, and D. R. Smith, "Spatially resolving antenna arrays using frequency diversity," J. Opt. Soc. Amer. A **33**, 899–912 (2016).

[47] T. Sleasman, M. F. Imani, W. Xu, J. Hunt, T. Driscoll, M. S. Reynolds, and D. R. Smith, "Waveguide-fed tunable metamaterial element for dynamic apertures," IEEE Antennas and Wireless Propag. Lett. **15**, 606–609 (2016).

[48] T. Sleasman, M. F. Imani, J. N. Gollub, and D. R. Smith, "Dynamic metamaterial aperture for microwave imaging," Appl. Phys. Lett. **107**, 204104 (2015).

[49] T. Sleasman, M. Boyarsky, M. F. Imani, J. N. Gollub,

and D. R. Smith, "Design considerations for a dynamic metamaterial aperture for computational imaging at microwave frequencies," J. Opt. Soc. Amer. B **33**, 1098–1111 (2016).

[50] R. C. Hansen, *Phased array antennas*, Vol. 213 (John Wiley & Sons, 2009).

[51] D. Sievenpiper, L. Zhang, R. F. J. Broas, N. G. Alexopolous, and E. Yablonovitch, "High-impedance electromagnetic surfaces with a forbidden frequency band," IEEE Transactions on Microwave Theory and techniques **47**, 2059–2074 (1999).

[52] D. F. Sievenpiper, J. H. Schaffner, H. J. Song, R. Y. Loo, and G. Tangonan, "Two-dimensional beam steering using an electrically tunable impedance surface," IEEE Transactions on Antennas and Propagation **51**, 2713–2722 (2003).

[53] A. W. Lohmann, R. G. Dorsch, D. Mendlovic, C. Ferreira, and Z. Zalevsky, "Space–bandwidth product of optical signals and systems," J. Opt. Soc. Amer. A **13**, 470–473 (1996).

[54] D. Claus, D. Iliescu, and P. Bryanston-Cross, "Quantitative space-bandwidth product analysis in digital holography," Applied optics **50**, H116–H127 (2011).

[55] N. Kaina, M. Dupré, G. Lerosey, and M. Fink, "Shaping complex microwave fields in reverberating media with binary tunable metasurfaces," Scientific reports **4** (2014).

[56] M. Dupré, P. del Hougne, M. Fink, F. Lemoult, and G. Lerosey, "Wave-field shaping in cavities: Waves trapped in a box with controllable boundaries," Physical review letters **115**, 017701 (2015).

[57] N. Kaina, M. Dupré, M. Fink, and G. Lerosey, "Hybridized resonances to design tunable binary phase metasurface unit cells," Optics express **22**, 18881–18888 (2014).

[58] P. del Hougne, F. Lemoult, M. Fink, and G. Lerosey, "Spatiotemporal wave front shaping in a microwave cavity," Phys. Rev. Lett. **117**, 134302 (2016).

[59] T. Sleasman, M. F. Imani, J. N. Gollub, and D. R. Smith, "Toward a tunable mode-mixing cavity for computational imaging (in press)," in *2016 IEEE International Symposium on Antennas and Propagation USNC/URSI National Radio Science Meeting* (2016) p. PP (in press).

[60] A. D. Yaghjian, "An overview of near-field antenna measurements," IEEE Trans. on Antennas Propag. **34**, 30–45 (1986).

[61] A. D. Yaghjian, "Approximate formulas for the far field and gain of open-ended rectangular waveguide," Antennas and Propagation, IEEE Transactions on **32**, 378–384 (1984).